

Research Paper

# Redox Responsive Hyaluronic Acid Nanogels for Treating RHAMM (CD168) Over-expressive Cancer, both Primary and Metastatic Tumors

Chenchen Yang, Cheng Li, Peng Zhang, Wei Wu and Xiqun Jiang✉

Department of Polymer Science &amp; Engineering, College of Chemistry &amp; Chemical Engineering, Nanjing University, Nanjing 210023, P. R. China.

✉ Corresponding author: Xiqun Jiang E-mail: jiangx@nju.edu.cn

© Ivyspring International Publisher. This is an open access article distributed under the terms of the Creative Commons Attribution (CC BY-NC) license (<https://creativecommons.org/licenses/by-nc/4.0/>). See <http://ivyspring.com/terms> for full terms and conditions.

Received: 2016.11.14; Accepted: 2017.01.02; Published: 2017.04.10

## Abstract

It remains a substantial challenge to targetedly deliver drug to both primary tumors and metastatic lesions employing a single nanoparticle delivery system. Here aiming at the receptor for hyaluronic acid mediated motility (RHAMM or CD168), a specific receptor for hyaluronic acid (HA), the bioreductive responsive HA nanogels loaded doxorubicin were prepared. The targeting effects of HA nanogels in high RHAMM-expressed cancer cells, primary and metastatic tumors were investigated. It was found that HA nanogels show a strong *in vitro* and *in vivo* RHAMM-mediated cellular uptake and drug delivery. The cellular uptake of HA nanogels in high RHAMM-expressed LNCaP and H22 cells was far more than the uptake in low RHAMM-expressed NIH3T3 cells. The IC<sub>50</sub> value of drug-loaded HA nanogels against H22 cells was lower than that of free drug. *In vivo* antitumor activity examinations showed that the HA nanogels not only had significantly superior antitumor efficacy in murine H22 and human LNCaP tumor-bearing mice but also exhibited much deep tumor penetration. The drug delivery of lymph node metastasis by systemically administering HA nanogels demonstrated that the HA nanogels could sufficiently increase drug concentration in metastatic lymph node by RHAMM-HA interaction and inhibit the growth of metastatic lymph node, even completely heal malignant lymph node metastasis. Thus, RHAMM-directed drug delivery is a promising therapy route for treating both primary and metastatic tumors.

Key words: nanogels, hyaluronic acid, RHAMM, reductive response, tumor metastasis, targeted therapies.

## Introduction

Targeted nanoparticle-based drug delivery systems which combine both passive and active targeting for cancer treatments have been intensely pursued over past three decades [1-3]. Based on the enhanced permeation and retention (EPR) effect against leaky tumor blood vessels and ligand-directed targeting, these drug delivery systems should be able to preferentially deliver therapeutic agents to tumor sites to improve therapy efficacy and reduce side effects. However, due to the complexity of tumor vascular system and receptor accessibility, the nanoparticle design and their *in vivo* performance remain great challenge for achieving high drug accumulation and antitumor efficacy.

Receptor for hyaluronic acid mediated motility (RHAMM), also called CD168, is a specific receptor for hyaluronic acid (HA). RHAMM is located in the cytoplasm, nucleus, and on the cell membrane [4,5]. It contributes to cells many biological functions, including cell motility [5,6], wound healing [7,8] and signal transduction [7,9]. In cancer cases, RHAMM is overexpressed in many solid tumors such as stomach [10], prostate [11], breast [12], colorectal cancers [13] and lung [14]. Besides, RHAMM is also the treated target of B-cell chronic lymphocytic leukemia, multiple myeloma and acute myeloid leukemia [15]. High expression of RHAMM has been correlated with tumor progression, invasion, and decreased survival

in patients. Further, RHAMM is found to link with metastatic dissemination of tumor [16, 17]. RHAMM has recently been suggested as a promising target for cancer immunotherapy [18]. Although RHAMM co-exists with CD44, another HA-specific receptor, in most cancers, there are 23% cancer cases with RHAMM overexpression in absence of CD44 [19]. Thus, it is urgent to develop RHAMM targeted therapeutic agents and systems. Currently, blocking the functions of RHAMM for example by peptides/antibodies is considered as a potentially therapeutic approach for RHAMM overexpressed cancers [20], and shows low toxicity in patients in clinical trial [18]. In addition, cell-based therapies using peptide vaccination have shown safe and effective at inducing CD8<sup>+</sup> RHAMM-specific T cell immune responses and antitumor activity in patients suffered from acute myeloid leukemia, myelodysplastic syndrome, multiple myeloma [15,21]. However, blocking RHAMM does not shown high therapy efficiency [22], and in turn, has the possibility to induce RHAMM expression in some cancer cases [23]. In addition, a decrease in specific T-cell responses was observed in some patients after peptide vaccination was stopped [24]. Alternately, using RHAMM-targeting nanoparticle as drug delivery systems may be a great option for RHAMM-overexpressed cancer treatment.

HA is a biocompatible, negatively charged linear polysaccharide, consisting of repeating units of *D*-glucuronic acid and *N*-acetyl-*D*-glucosamine. HA binds to its specific cell-surface receptors, including CD44, RHAMM, and intercellular adhesion molecule 1 (ICAM-1), to activate a lot of the transduction of intracellular signals [25]. Although it is well known that HA is the principle ligand of RHAMM [26], little is known about interactions between HA and RHAMM, and the behaviors of HA-based carriers in RHAMM overexpressed cells and tumors in the cases of independent of CD44. Moreover, the targeting and antitumor activity of HA-based drug delivery systems in the mice bearing RHAMM overexpressed tumor are rarely understood. Here, we are reporting a RHAMM target mediated drug delivery systems based on bio-reductive sensitive HA nanogels. By do so, the high structural stability of nanogels, the bio-reductive sensitive disulfide linkage and inherent biological activities of HA are integrated into one nano drug delivery system. We investigate the biological behaviors and drug delivery ability of HA nanogels *in vitro* and *in vivo* using different cell lines and tumors, including those murine and human cancer cells and tumors, in which RHAMM overexpression is dominant while CD44 expression is minor.

## Experimental

### Measurement of HA receptor expression of cells

2.5×10<sup>5</sup> LNCaP (human prostate cancer cell), H22 (Murine hepatic cell), A549 (human pulmonary carcinoma cell), and NIH3T3 (murine embryonic fibroblast cell) cells were seeded into each well of a 6-well plate with a coverslip and incubated for 24 h at 37 °C in cell incubator, respectively. Appropriate anti-mouse/human RHAMM (CD168) antibody was then added into the medium. After 1 h of co-incubation at 37 °C, the cells were adequately washed three times with PBS and a certain amount of FITC linked goat anti-rabbit secondary antibody was then added. After 0.5 h of co-incubation at 37 °C, the cells were washed three times with PBS. Then, Hoechst 33258 (Keygen Biotech. Co., Ltd.) was used to stain the cell nuclei of the cells. The treated cell samples were observed with CLSM (LSM 710, Zeiss, Germany). FITC and Hoechst 33258 were excited with a 488 nm argon laser and a 405 nm diode laser, respectively. We used western blot analysis to quantitatively analyze the expression index of RHAMM (CD168) and CD44 in LNCaP, H22, A549 and NIH3T3 cells. According to the previous work [27], 5×10<sup>6</sup>-1×10<sup>7</sup> cells were incubated with 300 μL lysing solution (10% Triton, 1 M Tris-HCl (pH 8.0), NaCl 4.0 g, 0.5 M EDTA, 0.1 M Orthovanadate, protease inhibitor cocktail (Complete (tm), Roche Diagnostics)) for 1 h at 0 °C on the ice. Then the lysing solutions were centrifuged (12000 rpm for 20 min) for collecting supernatant and the protein concentration confirmed by a commercial assay (Bio-Rad, Munchen, Germany). Equivalent of protein were separated by sodium dodecyl sulfate polyacrylamide gel electrophoresis (SDS-PAGE), and then were blotted onto nitrocellulose membranes (Immobilon Transfer Membrane, Millipore, USA). Blots were co-incubated with the primary anti-RHAMM(CD168) antibody 80-90 kDa RHAMM protein recognizing all splice variants or anti-CD44 antibody specific for approximately 85 kDa CD44 protein or anti-actin antibody (C-11, goat polyclonal IgG, Santa Cruz Biotechnologies, USA) specific for the 42 kDa actin protein overnight at 4 °C, respectively. Finally, blots were washed three times with buffer (Tris-buffered saline and 0.1% Tween 20) and co-incubated with peroxidase-linked secondary antibodies before observing in the chemiluminescence imaging system.

### Confocal microscopy imaging of cellular uptake

1 mL FITC solution (4 mg/mL) was added into a solution of MAHA (1.0 g/20 mL H<sub>2</sub>O) and the

solution was reacted overnight in dark. Next, the mixture was purified by precipitating and washed twice. Subsequently, the product of fluorescence labeled MAHA was dried overnight in dark. The preparation of FITC-labeled HAAss nanogels was based on the FITC-labeled MAHA. Then, for cellular uptake exploration,  $2.5 \times 10^5$  LNCaP, H22, A549 and NIH3T3 cells were seeded into each well of 6-well plate with coverslip respectively and incubated for 24 h until cells attachment at 37 °C in cell incubator. 200  $\mu$ L of FITC-labeled HAAss nanogels was then added into each well. After 4 h of co-incubation at 37 °C, the cells were washed with PBS for three times. The cell nucleus was dyed by Hoechst 33258. Then we used the CLSM to observe cells. For co-localization analysis, the LNCaP cells samples were divided into two groups. Half of cells were treated with anti-RHAMM antibody for 1 h before used. The two groups of cells were treated with 100 nM Lyso-Tracker Red for 30 min at 37 °C, and then were incubated with 200  $\mu$ L of FITC-labeled HAAss nanogels for 4 h at 37 °C. The cells were observed under CLSM. Lyso-Tracker Red was excited with a 543 nm HeNe laser.

### Flow cytometry examination

The LNCaP, H22, A549 and NIH3T3 cells ( $2.5 \times 10^5$  cells per well) were seeded into a 6-well plate without coverslip and incubated for 24 h in cell incubator. Then these cells were incubated with 200  $\mu$ L of FITC-labeled HAAss nanogels for another 4 h at 37 °C. The adherent cells were washed three times with PBS. The cells (except H22) were trypsinized by 0.25% trypsin solution (Hyclone, Waltham, USA) for 5 min. The fluorescence intensity of the cell suspension was detected at 488/525 nm with a fluorescence-activated cell sorting (FACS) (BD, Biosciences, USA).

### Anti-RHAMM and anti-CD44 antibody blocking

LNCaP and H22 cells were pre-incubated with or without anti-RHAMM antibody diluted in 1 ml RPMI-1640 (without FBS) for 1 h at 37 °C, and then all samples were co-cultured with 200  $\mu$ L of FITC-labeled HAAss nanogels for 4 h at 37 °C and washed with PBS 3 times before being measured on CLSM and FACS.

A549 cells were pre-incubated with single anti-CD44, single anti-RHAMM or double antibody diluted in 1 ml RPMI-1640 (without FBS) for 1 h at 37 °C, and then all samples were co-cultured with 200  $\mu$ L of FITC-labeled HAAss nanogels for 4 h at 37 °C and washed with PBS 3 times before being measured on CLSM.

### Co-localization of HAAss nanogels and RHAMM of cells

RBITC-labeled HAAss nanogels were prepared as follows: 2 mL of HAAss nanogels solution was reacted with 70  $\mu$ L RBITC (5 mg/mL in DMSO) at 25 °C in dark overnight. Then, the dye-labeled nanogels were purified by centrifugation at 16000 rpm for 90 min. The obtained solid was washed to remove the unreacted RBITC and re-dispersed in PBS.

LNCaP cells were first incubated with 200  $\mu$ L of RBITC labeled HAAss nanogels for 4 h at 37 °C, and were washed three times with PBS. The adherent cells LNCaP were co-cultured with anti-RHAMM (CD168) antibody for 1 h and FITC linked goat anti-rabbit secondary antibody for 0.5 h in sequence at 37 °C. Then the cells were washed with PBS. The cell nucleus was dyed as above. Then the cells were observed with CLSM. RBITC were excited with a 543 nm HeNe laser. We also used FACS to quantitative analyze at the same method above.

### Establish H22 and LNCaP non-metastatic tumor models

The left flank of each ICR male mouse (20-25 g) was inoculated with  $4 \times 10^6$  H22 cells subcutaneously. These mice were fed for 7 days before used. Analogously,  $1 \times 10^6$  LNCaP cells were subcutaneously inoculated into the right flank of each BALB/c male nude mouse (15-20 g) and continuously fed them for three weeks before used. All the animal experiments were compliance with the Chinese animal use and care committee and carried out ethically and humanely.

### In vivo experiments in H22 non-metastatic tumor model

For exploring the distribution of DOX *in vivo*, we divided the mice with H22 tumor into 8 groups randomly (3 mice in each group). One of them was served as no-treatment group. The mice of treatment groups were sacrificed at different time post-injection with DOX-loaded HAAss nanogels (4.5 mg/kg DOX eq.). The organs or the tissues like the heart, liver, spleen, lung, kidney and tumor were cut up, washed with de-ionized water and dehydrated with filter paper. Blood were centrifuged at 10000 rpm for blood plasma. The DOX in each tissue was extracted with immersing in 4 mL extract liquor (70% (v/v) alcohol solution with 0.3 M HCl) for 48 h. The extract liquor was obtained with centrifugation for 10 min. Finally, the fluorescence intensity of DOX in extract liquor was measured by fluorescence spectroscope (Shimadzu, RF-5301PC, Japan) (480/560 nm). All corresponding sample of the experimental groups deducted the mean values of each tissue from the

no-treatment group. The % ID/g was calculated by Equation 1:

$$\%ID/g = \text{DOX amount in tissue} / (\text{tissue weight} \times \text{injected dose}) \times 100\% \quad (1)$$

For tumor penetration analysis, tumor tissues of mice with H22 tumor were obtained at 1 h, 6 h, 24 h after intravenous (i.v.) injection of 300  $\mu\text{L}$  FITC-HAss nanogels. Then the tumors were immersed in 4% paraformaldehyde and 30% sucrose, respectively. Next, they were frozen in optimum cutting temperature compound (O. C. T.) embedding medium. 10  $\mu\text{m}$  sections were obtained by using a cryostat (Leica CM 30505). For immunostaining, the sections were rehydrated in PBS and then incubated with 3% BSA for 1 h at 37 °C. Then a certain amount of primary antibody (1: 200, rat monoclonal anti-mouse CD31, BD Pharmingen, San Jose, California) was used to stain the sections. After washed with PBS, The sections were then counterstained with an Alexa 594 linked secondary antibody (1: 1000, donkey anti-rat, Molecular Probes, Eugene, OR) and DAPI (Keygen Biotech. Co., Ltd.), respectively. At last, the coverslips were detected by CLSM [28].

To affirm the expression of RHAMM in tumor tissue and the co-localization of nanogels and RHAMM, The H22 non-metastatic tumor-bearing mice were sacrificed at 24 h after i.v. injection with RBITC labeled HAss nanogels. Then, the tumor tissue sections were obtained as above. To visualize tumor RHAMM expression and co-localization with HAss nanogels, tissue sections were stained with anti-RHAMM antibody as primary antibody and FITC linked goat anti-rabbit antibody as secondary antibody. After washed with PBS for three times, the sections were stained with DAPI for 30 min. Finally, the prepared slides were observed with CLSM.

*In vivo* antitumor efficacy analysis, 50 mice with H22 tumor (tumor volume around 50  $\text{mm}^3$  after inoculated with cancer cells for 7 days) were divided into 5 groups (10 mice in each group) randomly. And then these mice were administered intravenously with 300  $\mu\text{L}$  of saline, empty HAss nanogels, free DOX (4.5 mg/kg), DOX-loaded HAss nanogels (4.5 mg/kg DOX eq.), and DOX-loaded HAcc nanogels (4.5 mg/kg DOX eq.), respectively, and the administered day was designed as the first day. The tumor size and body weight of each mouse were measured every other day until the 15<sup>th</sup> day. The tumor volume was calculated by Equation 2:

$$\text{Tumor volume (V)} = 1/2 D \times d^2 \quad (2)$$

In this equation, *D*, *d* and *V* represent the maximum, minimum diameters and volume of the tumor, respectively. The tumor growth inhibition

(TGI) was calculated by Equation 3 [29].

$$\text{TGI} = (\text{V of saline group} - \text{V of test group}) / (\text{V of saline group}) \times 100\% \quad (3)$$

*V* is defined as the average volume of the tumor.

### **In vivo experiments in LNCaP non-metastatic tumor model**

The bio-distribution of HAss nanogels in LNCaP tumor-bearing nude mice was measured as follow: 3 mL of HAss nanogels suspension (5 mg/mL) was mixed with 70  $\mu\text{L}$  of NIR-797 isothiocyanate solution (6 mg/mL) and the mixture was reacted for 24 h in dark. The resultant mixture was centrifuged twice to remove the unreacted NIR-797. Then the NIR-797-labeled HAss nanogels were re-dispersed in PBS. LNCaP tumor-bearing nude mice were i.v. injected with 300  $\mu\text{L}$  of NIR-797-labeled HAss nanogels. Then the images were acquired at different time by NIR imaging until 24 h post-injection. Then, to semi-quantitatively explore the uptake ratio of HAss nanogels in each organ, we performed the region of interest (ROI) analysis based on *ex vivo* organic fluorescence images. Briefly, we used NIR imaging to confirm the relationship between fluorescence intensity and weight of NIR797 HAss nanogels. Then the NIR fluorescence intensity and weight of each organ were obtained. The final data were presented as % ID/g.

According to the data above, the permeability of HA nanogels in H22 tumor is great. To validate the great permeability of HA nanogels in LNCaP tumor, we used *in vivo* CLSM technique. Briefly, LNCaP tumor-bearing mouse was anesthetized by an inhalational anaesthesia system (IAS), and then intravenously injected with a certain RBITC-labeled HAss nanogels. After 5 min post-injection, the tumor of live mouse was placed on platform of CLSM and kept motionless during the period of signal acquisition. Then the real time location of HA nanogels and blood vessel were acquired and the quantitative data were obtained by CLSM with 20 $\times$  objective and shown by profile mode of ZEISS and matrix graph of Origin.

Similarly, to confirm the locations of RHAMM and HAss nanogels in tumor *ex vivo*, the LNCaP tumors were treated in the same method as H22 tumors, and then the CLSM images of immunofluorescence sections were obtained.

To verify the *in vivo* antitumor activity of DOX-loaded HAss nanogels, 18 LNCaP tumor-bearing nude mice (tumor volume around 100  $\text{mm}^3$  after inoculated with cancer cells for 3 weeks) were grouped (6 mice in each group) randomly. The tumor-bearing nude mice were i.v. administered with

300  $\mu\text{L}$  of saline, free DOX (4.5 mg/kg), DOX-loaded HAAss nanogels (4.5 mg/kg DOX eq.) respectively, and this administered day was designed as the first day. The body weight and tumor size were recorded every other day until 15<sup>th</sup> day like the mice with H22 tumor. The tumor volume and the TGI were calculated by Equation 2 and Equation 3, respectively.

### Establish Metastatic Tumor Model.

0.1 mL ( $5 \times 10^5$ ) H22 cells were injected subcutaneously on the left hind foot sole of each ICR male mouse. 21 days after tumor inoculation, mice with swollen inguinal lymph node were selected and used in our experiments. At that time a number of H22 tumor cells had invaded the sentinel lymph node.

### In vivo experiments in H22 metastatic tumor model

To explore the permeability of HA nanogels in lymph node, we used *ex vivo* CLSM technique. Briefly, H22 metastatic tumor mouse was intravenously injected with a certain RBITC-labeled HAAss nanogels. After 2 h post-injection, the metastatic lymph node and normal lymph node of mouse were exteriorized and rapidly placed on platform of CLSM. Then the microdistribution of HA nanogels were acquired were obtained by CLSM with 10 $\times$  objective.

To further prove that HA nanogels can enter into metastatic lymph node and carry DOX into it, we utilized near-infrared (NIR) imaging technique. Above metastatic tumor-bear mice were i.v. injected with 300  $\mu\text{L}$  of NIR-797-labeled HAAss nanogels. Then, real time *in vivo* bio-distributions of HAAss nanogels in primary tumor and left inguinal lymph node were explored at different time points by using NIR imaging. As above, 3 of 15 H22 metastatic tumor-bear mice were chose as no-treatment group, and the rest of mice were grouped randomly (3 mice in each group). Two of them were treated with free DOX (4.5 mg/kg) and other two groups were injected with DOX-loaded HAAss nanogels intravenously (4.5 mg/kg DOX eq.). Then the mice were sacrificed at 12 h and 24 h post-injection administration, respectively. The left swollen inguinal lymph node and right normal inguinal lymph node were exteriorized and treated as above experiments of bio-distribution. Next, the data of DOX distribution in lymph node were obtained by fluorescence spectroscopy.

Histology analysis was carried out as follow, the swollen inguinal lymph node were fetched out from sacrificed H22 metastatic tumor-bearing mice and performed at the same methods as the tumor of H22 non-metastatic tumor model. Finally, the slides were observed by CLSM.

For the inhibition of lymphatic metastasis

evaluation, 27 metastatic tumor-bearing mice (14 days after tumor inoculation) were divided into 3 groups (9 mice in each group) randomly. 300  $\mu\text{L}$  of saline, free DOX (4.5 mg/kg) and DOX-loaded HAAss nanogels (4.5 mg/kg DOX eq.) were injected intravenously, respectively. 3 mice of each group were sacrificed and left inguinal lymph nodes were taken out at 7<sup>th</sup> day, 14<sup>th</sup> day and 21<sup>st</sup> day after post-injection administration. 3 mice were sacrificed at the injection administration day to obtain lymph node before treatment. In addition, in order to prove the therapeutic effect of DOX-loaded HAAss nanogels in malignant metastasis, other 18 mice with lymphatic metastasis (6 mice in each group) were treated as the same methods to acquire the survival rate of each group.

The volume of lymph node was calculated by Equation 2 and the TGI was calculated by Equation 3.

The tumor growth rate (TGR) was calculated by Equation 4 [30].

$$\text{TGR} = \frac{\text{(The lymph V after treatment)}}{\text{(The lymph V before treatment)}} \quad (4)$$

The V represents the average volume of the lymph node.

### Statistical analysis

Quantitative data were shown as mean  $\pm$  standard deviation (s.d.). Statistical comparisons were performed by one-way ANOVA analysis and Student's *t*-test. *P* value < 0.05 was considered statistically significant.

## Results and discussions

### Preparation and characterization of HA nanogels

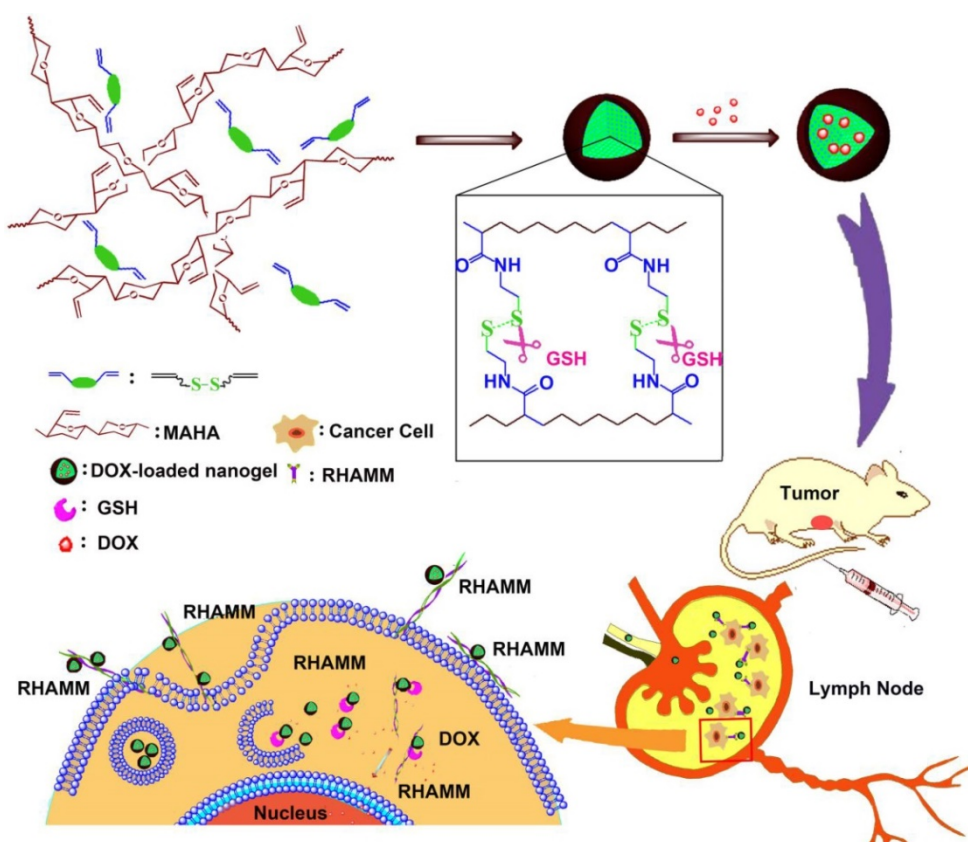
The bio-reductive sensitive HA nanogels were prepared by modifying HA with vinyl group, followed by copolymerizing with disulfide linkage-contained cross-linker, cystamine bisacrylamide (CBA), in aqueous medium (Scheme 1 and Scheme S1). The incorporation of disulfide linkage into the nanogels endows the carrier with redox-sensitive property. The structure of intermediates and HA nanogels was confirmed by <sup>1</sup>H NMR and FT-IR measurements (Fig. S1-S3). In Fig. S3, the main absorption bands of FT-IR at 3287  $\text{cm}^{-1}$  for the hydroxyl (OH) of MAHA, 1557  $\text{cm}^{-1}$  for the amide (NHC=O) of CBA prove that the nanogels are formed of MAHA and CBA. For comparison, non-bio-reductive sensitive HA nanogels were also synthesized by using disulfide linkage-free *N,N'*-methylene bisacrylamide (MBA) as cross-linker (Scheme S1). The heterogeneous distribution of hydrophobic cross-linker units in meshed network,

due to the polymerization of the cross-linkers themselves, drives the formation of HA nanogels [31, 32]. These two types of nanogels are designed into HAss and HAcc nanogels for disulfide linkage-contained and free ones, respectively. Dynamic light scattering (DLS) and  $\zeta$ -potential measurements show that the size of HAss and HAcc nanogels is  $79.1 \pm 3.2$  nm and  $66.3 \pm 3.4$  nm in PBS solution (10 mM, pH = 7.4), respectively (Fig. 1A and 1B), while the  $\zeta$ -potential of two nanogels is about -40.0 mV. Transmission electron microscopy (TEM) images show that HAss and HAcc nanogels have a spherical morphology and the average size of HAss and HAcc nanogels by TEM is  $68.9 \pm 7.9$  nm and  $57.3 \pm 7.8$  nm, respectively, which are slightly smaller than the data from DLS owing to the dehydration of the HA nanogels in TEM (Fig. 1C and 1D). To investigate the stability of HA nanogels in physiological environments, the hydrodynamic diameter and light scattering intensity of HAss nanogels in 30% inactivated fetal bovine serum (FBS) solution and bovine serum albumin (BSA) solution with different concentrations were detected by DLS, respectively. The HAss nanogels are highly stable within the 120 h of observation period and display no obvious fluctuation in the diameter and light scattering intensity in these protein-contained media (Fig. 1E

and Fig. S4).

### GSH-triggered degradation of HA nanogels

HAss nanogels are expected to be stable in circulation system and extracellular space, but cleavable in tumor cells where the concentration of reductant GSH is about 4-fold higher than that in normal tissues [33, 34]. Thereby, we examined the reduction-responsive behaviors of the HAss nanogels in the aqueous solutions with 1 mM, 10 mM and 40 mM GSH. As shown in Fig. 1F, the light scattering intensity of sample shows a monotonous decrease with time in both aqueous solutions with 10 mM and 40 mM GSH. In contrast, the size of HAss nanogels is nearly constant in 10 mM and 40 mM GSH solution (Fig. 1G). These results indicate that nanogels de-integrate and the number of intact nanogels decrease due to the cleavage of disulfide linkage under the action of GSH. On the other hand, the nanogel size and the light scattering intensity is nearly unchanged in 1 mM GSH solution which is approximate to the concentration of normal tissues. The GSH-triggered degradation of nanogel particles is also confirmed by TEM (Fig. 1H). The nanogels particles either de-integrate or become loose after treatment with 10 mM GSH for 24 h.



**Scheme 1.** The preparation of HAss nanogels and the targeting of HAss nanogels to RHAMM in cancer cell and lymph node which contains cancer cells with RHAMM overexpression.

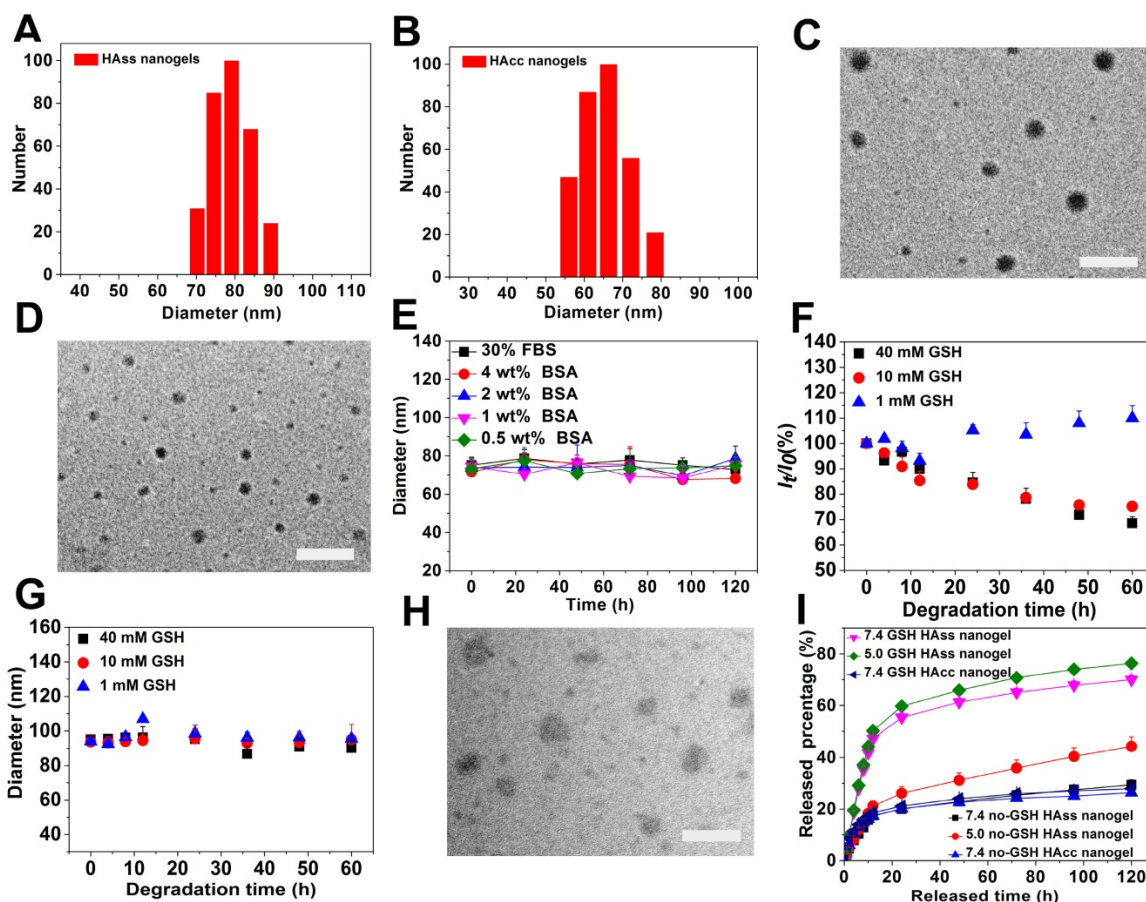


**Figure 1.** The DLS plot of (A) HAss nanogels and (B) HAcc nanogels. TEM images of (C) HAss nanogels and (D) HAcc nanogels. The scale bar is 200 nm. (E) The diameter stabilities of HAss nanogels in FBS and BSA solutions (mean  $\pm$  s.d., n = 3). (F) Light scattering intensity ratio  $I_t/I_0$  of HAss nanogels in the presence of 1 mM, 10 mM and 40 mM GSH, respectively against degradation time.  $I_0$  and  $I_t$  are the light scattering intensity at degradation time  $t = 0$  and  $t = t$ , respectively. (G) The plot of HAss nanogels diameter change with degradation time (mean  $\pm$  s.d., n = 3). (H) TEM image of HAss nanogels after treated with 10 mM GSH for 24 h. The scale bar is 200 nm. (I) *In vitro* release plot of DOX from HAss nanogels (pH = 5.0, 7.4) and HAcc nanogels (pH = 7.4) in PBS at 37 °C with or without GSH, respectively (mean  $\pm$  s.d., n = 3).

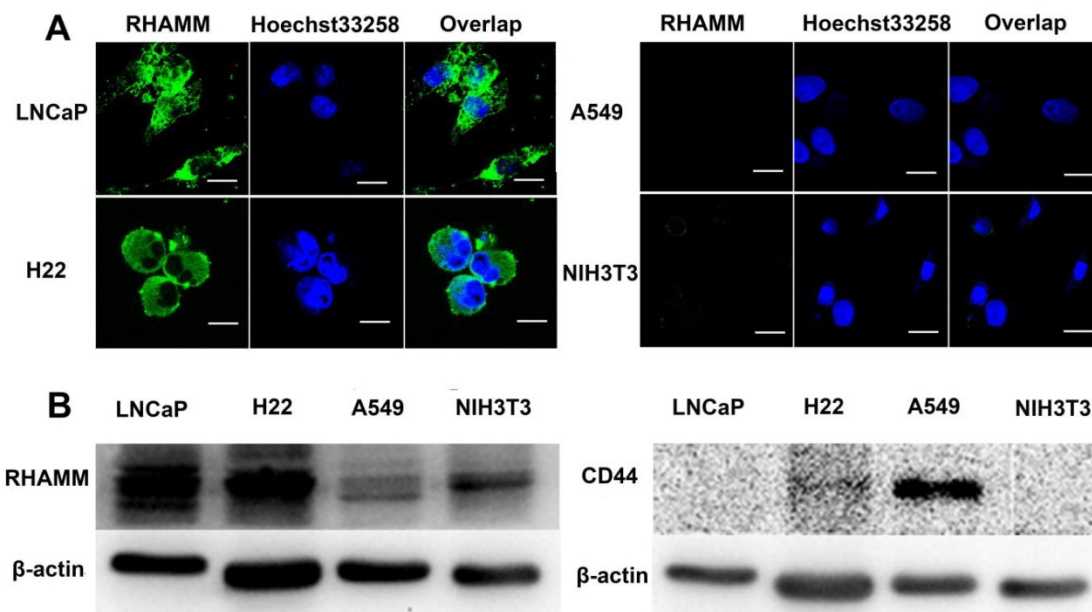


**Figure 2.** (A) The RHAMM expression in LNCaP, H22, A549 and NIH3T3 cell lines were detected by CLSM, respectively. The green areas represent RHAMM. The scale bar is 20  $\mu$ m. (B) The RHAMM and CD44 expression of cells were quantified by Western Blotting.

## Drug loading and release in HA nanogels

To assess the drug loading capacity and release behavior of DOX loaded in HA nanogels, doxorubicin (DOX) was chosen as a model drug. DOX were loaded in HA nanogels by an incubation method utilizing the electrostatic interactions between the amino groups of DOX and carboxyl groups in HA nanogels. The hydrodynamic diameters of DOX-loaded HAss and HAcc nanogels were determined to be  $52.4 \pm 3.4$  nm and  $54.9 \pm 3.6$  nm by DLS respectively (Fig. S5 and S6), and the  $\zeta$ -potential were  $-30.12 \pm 3.12$  mV and  $-27.27 \pm 3.21$  mV. The size reduction of nanogels possible because of the decreasing electrostatic repulsive-force inside the DOX loaded nanogels. The DOX loading content (LC) of DOX in HAss nanogels is 24% and the encapsulation efficiency (EE) reaches 88%. While for HAcc nanogels, EE and LC is 66% and 17%, respectively. Fig. 11 displays the release plot of DOX from HAss and HAcc nanogels in different pH media with or without 10 mM GSH at 37 °C *in vitro*. In the PBS without GSH, only about 20% and 26% of DOX loaded is released from the HAss nanogels at pH of 7.4 and 5.0 within 24 h, respectively, and there is no further release of DOX until 120 h. By contrast, the release amount of DOX from the HAss nanogels increases sharply to about 69% and 76% at pH 7.4 and 5.0 within 120 h, respectively, in the presence of GSH (10 mM). On the other hand, no speeding DOX release from HAcc nanogels is observed in the GSH-contained medium. This result indicates that the release process is accelerated by delinking disulfide bond with GSH.

## RHAMM and CD44 in cells

To correlate the cellular overexpressed RHAMM with cytotoxicity and cellular uptake of nanogels, we examined RHAMM and CD44 expression in LNCaP (human prostate cancer), H22 (murine hepatoma), A549 (human pulmonary cancer) and NIH3T3 (fibroblast) cells using fluorescence antibody stain and Western Blot analysis. From the images of confocal laser scanning microscopy (CLSM), it is found that the fluorescence intensity in LNCaP and H22 cells is far stronger than that in A549 and NIH3T3 cells (Fig. 2A), indicating that the expression of RHAMM in LNCaP and H22 cells is far more than that in A549 and NIH3T3 cells. The Western Blot data further indicate that RHAMM is over-expression in LNCaP cells and H22 cells, and low-expression in A549 and NIH3T3 cells, while CD44 is only over-expression in A549 cells, and low-expression in LNCaP, H22 and NIH3T3 cells (Fig. 2B).

## Cytotoxicity and cellular uptake

Next, we evaluated the cytotoxicity of drug-loaded HAss nanogels in these cells using DOX as positive control. The cell viability rates of the DOX-loaded HAss nanogels and free DOX against LNCaP, H22, A549 and NIH3T3 cells are displayed in Fig. 3A-3D, respectively. We find a dose dependent cytotoxicity for both the free DOX and DOX-loaded HAss nanogels in these cells. Similar behaviors are also observed in DOX-loaded HAcc nanogels (Fig. S7-S10). According to the calculation result (Fig. S11), the  $IC_{50}$  of DOX-loaded HAss nanogels against A549 cell and NIH3T3 cell is  $4.97 \mu\text{g/mL}$  and  $8.80 \mu\text{g/mL}$ , respectively, both are higher than these of free DOX,  $2.85 \mu\text{g/mL}$  and  $4.25 \mu\text{g/mL}$ , respectively. These data mean that the cytotoxicity of DOX-loaded HAss nanogels is lower than that of free DOX in A549 and NIH3T3 cells. Interestingly, the cytotoxicity of DOX-loaded HAss nanogels against H22 cells ( $IC_{50} = 7.71 \mu\text{g/mL}$ ) is significantly higher than that of free DOX ( $IC_{50} = 11.22 \mu\text{g/mL}$ ), and it ( $IC_{50} = 5.37 \mu\text{g/mL}$ ) is almost equal to that of free DOX ( $IC_{50} = 4.89 \mu\text{g/mL}$ ) for LNCaP cells. This is most likely to attribute to the combination effect of overexpressed RHAMM-mediated cellular uptake and bio-reductive activity of HAss nanogels in these two kinds of cells. The cytotoxicity of DOX-loaded HAcc nanogels against all four cell lines is lower than that of free DOX (Fig. S7-S10) due to the lower release rate of DOX from more stable HAcc nanogels in reductive environment. In addition, no cytotoxicity is observed for the empty HA nanogels against both cancer cells and normal cell (human hepatocyte cell line, L-02) (Fig. S12 and S13).

Because the performance of HAss nanogels is much better than that of HAcc nanogels in reductive responsive drug release and cytotoxicity, we mainly used HAss nanogels as a preferential drug delivery carrier in following experiments. We used the CLSM and FACS to assess the cellular uptake and intracellular distribution of HAss nanogels. The green fluorescence signals of the labeled HAss nanogels are obvious in the cytoplasm after co-incubation for 4 h (Fig. 4A), demonstrating that HAss nanogels can be efficiently bound and internalized by LNCaP and H22 cells. However, there is nearly no fluorescence signal derived from nanogels in NIH3T3 cells. For A549 cells, the uptake of HAss nanogels is also existed. To quantitatively assess cellular uptake of HAss nanogels in LNCaP (over-expression RHAMM), H22 cells (over-expression RHAMM) and NIH3T3 cells (low-expression RHAMM), FACS measurement was employed. According to the Fig. 4B, the median fluorescent intensity (MFI) in LNCaP and H22 cells is

about 3.1- and 2.4-folds higher than that in NIH3T3 cells, respectively. That means the uptake of HAss nanogels in LNCaP and H22 cells is more remarkable

than that in NIH3T3 cells. Apparently, the cellular internalization of HAss nanogels is connected with the RHAMM-mediated cellular uptake.

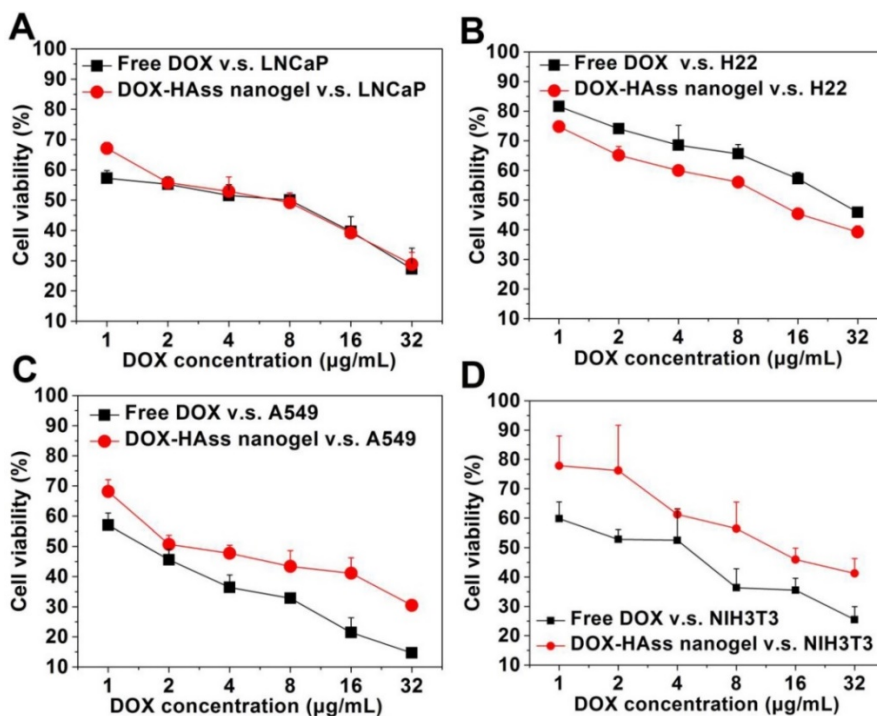


**Figure 3.** *In vitro* cytotoxicity of free DOX and DOX-loaded HAAss nanogels against (A) LNCaP, (B) H22, (C) A549 and (D) NIH3T3 cell lines after 24 h incubation, respectively (mean ± s.d., n = 3).

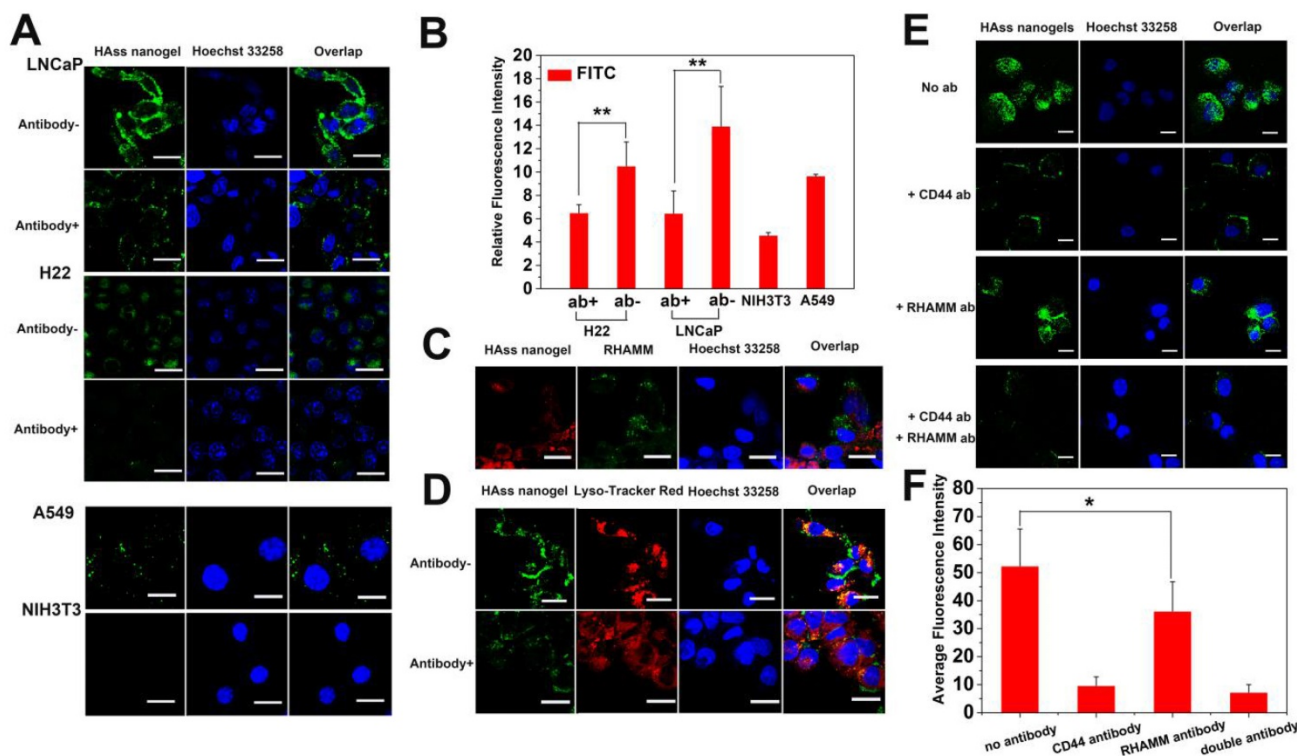


**Figure 4.** (A) CLSM images of LNCaP, LNCaP treated with anti-RHAMM antibody, H22, H22 treated with anti-RHAMM antibody, A549 and NIH3T3 cells incubated with FITC labeled HAAss nanogels (green), respectively. (B) Quantitative analysis of the difference of FITC intensity in LNCaP and H22 with or without anti-RHAMM antibody (ab), A549 and NIH3T3 cells, respectively (mean ± s.d., n = 3). \* represents  $P < 0.05$ . (C) CLSM images of co-localization between HAss nanogels (red) and anti-RHAMM antibody (green). (D) The co-localization of FITC labeled HAss nanogels and lysosome in LNCaP (up) and LNCaP treated with anti-RHAMM antibody (bottom). (E) The uptake of HAss nanogels (green) in A549 treated with different antibody. (F) Semi-quantitative analysis of uptake in A549 treated with different antibody based on CLSM image. The nuclei were stained with Hoechst 33258 (blue). The scale bar in each picture is 10 µm.

To further investigate RHAMM-mediated cellular uptake, a competition assay was performed. Firstly, LNCaP and H22 cells were pre-incubated with or without anti-RHAMM antibody, respectively. Then, a certain amount of FITC-labeled HAAss nanogels was incubated with above cells. The qualitative analysis and quantitative analysis were performed by CLSM and FACS. As shown in Fig. 4A, the green fluorescence signals in LNCaP and H22 cells pre-incubated with antibody are obviously less than those without antibody treatment. The FACS data further support this result ( $P < 0.05$ , Fig. 4B). Reversely, the LNCaP cells were initially co-cultured with RBITC-labeled HAAss nanogels for 4 h and then treated with anti-RHAMM antibody and FITC conjugated secondary antibody. The signals of anti-RHAMM antibody in the cells pre-incubated with HAAss nanogels, as shown in Fig. 4C and the Fig. S14, are much less than these without HAAss nanogels treatment (Fig. 2A), indicating the competitive relationship between HA nanogels and antibody. Interestingly, the RBITC-labeled HAAss nanogels do not co-localize with FITC-labeled antibody in the cells with such treatment, as shown in Fig. 4C, demonstrating the competitive relationship between HA nanogels and antibody again. The co-localization of HAAss nanogels with Lyso Tracker (red), an endosomal/lysosomal marker, in LNCaP cells suggests that RHAMM-mediated cellular uptake is an endocytosis process (Fig. 4D). To explore the relationship between CD44 and RHAMM in cell uptake, we used A549 cell as a control, which has overexpressed CD44 and a low level expressed RHAMM. We treated cells with anti-CD44, anti-RHAMM or both antibodies before uptake test, respectively. As shown in Fig. 4E, we can see that the cellular uptake of HAAss nanogels decreases drastically after the cells are treated by anti-CD44 antibody, indicating that CD44 receptors also play important role in the uptake of HAAss nanogels. However, due to the expression of RHAMM in the cells, there is more signals in anti-CD44 antibody treated cells compared to the both antibodies (anti-CD44 and anti-RHAMM antibodies) treated cells. Moreover, the cellular uptake of HAAss nanogels decreases slightly in anti-RHAMM antibody treated cells (Fig. 4F,  $P < 0.05$ ). These results suggest that even in CD44-predominant A549 cell, the RHAMM is also working in binding and uptake HAAss nanogels.

### **In vivo behavior of HA nanogels in H22 non-metastatic tumor model**

It is reported that limited chemotherapy efficacy in cancer treatment is often associated with poor drug penetration in tumor, especially in nanomedicine-

based treatment. Thus, we evaluated the penetration ability of HAAss nanogels in tumor tissue. The FITC-labeled HAAss nanogels were injected into the mice with H22 tumor intravenously, and observed the location of the labeled HAAss nanogels relative to tumor vessels in tumor slices. The red fluorescence signal and green fluorescence signal represent the location of tumor blood vessels and FITC-labeled HAAss nanogels, respectively. It is found that in tumor tissue, HAAss nanogels gradually spread far away from blood vessels as time escapes post-injection (Fig. 5A). Compare to 1 h and 6 h after injecting, a lot of HAAss nanogels are diffused into a more extensive area in tumor tissues and penetrate much farther from blood vessels at 24 h after i.v. injection, suggesting that HAAss nanogels own outstanding ability in tumor penetration. To correlate the behavior of HAAss nanogels in the tumor with the expression of RHAMM in H22 tumor, immunofluorescence staining was performed. As shown in Fig. 5B, the expression of RHAMM (green) in H22 tumor are much high, and many RBITC-labeled HAAss nanogels (red) can be found in tumor section at 24 h post-injection. The co-localization of green RHAMM with red HAAss nanogels shows that all nanogels are bound with RHAMM (Fig. 5B), indicating the RHAMM targeting behavior of HA nanogels in H22 tumor.

The bio-distribution of drug *in vivo* is a vital indicator of the performance of drug delivery for nanoparticles. Thus, we detected the DOX bio-distribution in the mice with H22 tumor after i.v. injection of DOX-loaded HAAss nanogels (4.5 mg/kg DOX eq.), and DOX concentrations in different organs and tissues were measured by spectrofluorometric method. We can see that for HAAss nanogels, the accumulation of DOX in tumor is about 7.5% of injection dose per gram (% ID/g) of tissue at 4 h post-injection and maintains at about 2.4% in the 72 h (Fig. 5C). The half-life time ( $t_{1/2}$ ) of DOX is 4.9 h for DOX-loaded HAAss nanogels. Compared to free DOX in the same model animal and same injection dose [37], the HA nanogels provide 7-8 folds increase in tumor drug concentration, and 4-fold longer drug half-life time. Thus, these results suggest that HAAss nanogels can carry more DOX into the tumor due to the passive targeting and active targeting. In addition, the relatively higher concentration of DOX is detected in the kidney and liver in the initial 1-4 h, the peak values of DOX in kidney and liver in the experimental period are about 11.7% ID/g and 10.8% ID/g, respectively. In the heart, the maximum DOX concentration is 4% ID/g. This value is much less than that of free DOX [35], indicating that the delivery of nanogels contributes to reducing the cardiotoxicity of DOX. The biodistribution data of DOX-loaded HAAss

nanogels show that the nanogels have a lower DOX concentration in the tumor (Fig. S15), compared to DOX-loaded HAss nanogels.

To evaluate antitumor efficacy of HA nanogel formulation *in vivo*, DOX-loaded HAss nanogels and HAcc nanogels were i.v. injected into the mice with H22 tumor (4.5 mg/kg DOX eq.). As controls, free DOX (4.5 mg/kg), HAss nanogels blank and saline were also i.v. injected into the mice. According to the tumor volume obtained every other day (Fig. 5D), the tumors grow promptly in the groups treated with blank and saline, while free DOX group displays a certain extent of antitumor activity with about 50 folds increase in volume of tumor on the 15<sup>th</sup> day post-injection (v.s. 1<sup>st</sup> day). On the other hand, the obvious inhibitions of tumor growth are found in the group dealt with DOX-loaded HAss nanogels. On the 15<sup>th</sup> day, the tumor size shows only 9 folds increase, and the growth of tumor tends to stop. The

differences of tumor volume among the DOX-loaded HAss nanogels group, saline group ( $P < 0.01$ , Fig. 5D) and free DOX group ( $P < 0.01$ , Fig. 5D) are highly significant. DOX-loaded HAcc nanogels also show sufficiently antitumor activity. The tumor volume of DOX-loaded HAcc nanogels group increases about 38 folds on the 15<sup>th</sup> day (v.s. 1<sup>st</sup> day). The values of TGI for DOX-loaded HAss, HAcc nanogels and free DOX are 98%, 85%, 75%, respectively. We think that the excellent antitumor activity of DOX-loaded HAss nanogels is owed to the strong RHAMM targeting, higher DOX permeation and accumulation, larger RHAMM-mediated uptake of H22 cells and GSH-triggered disulfide linkage cleavage of the nanogels. In addition, the well-toleration for these nanogels formulations is observed based on the body weigh monitoring (Fig. 5E). These results demonstrate that DOX-loaded HAss nanogels can observably enhance the therapeutic effect of anti-cancer drug.

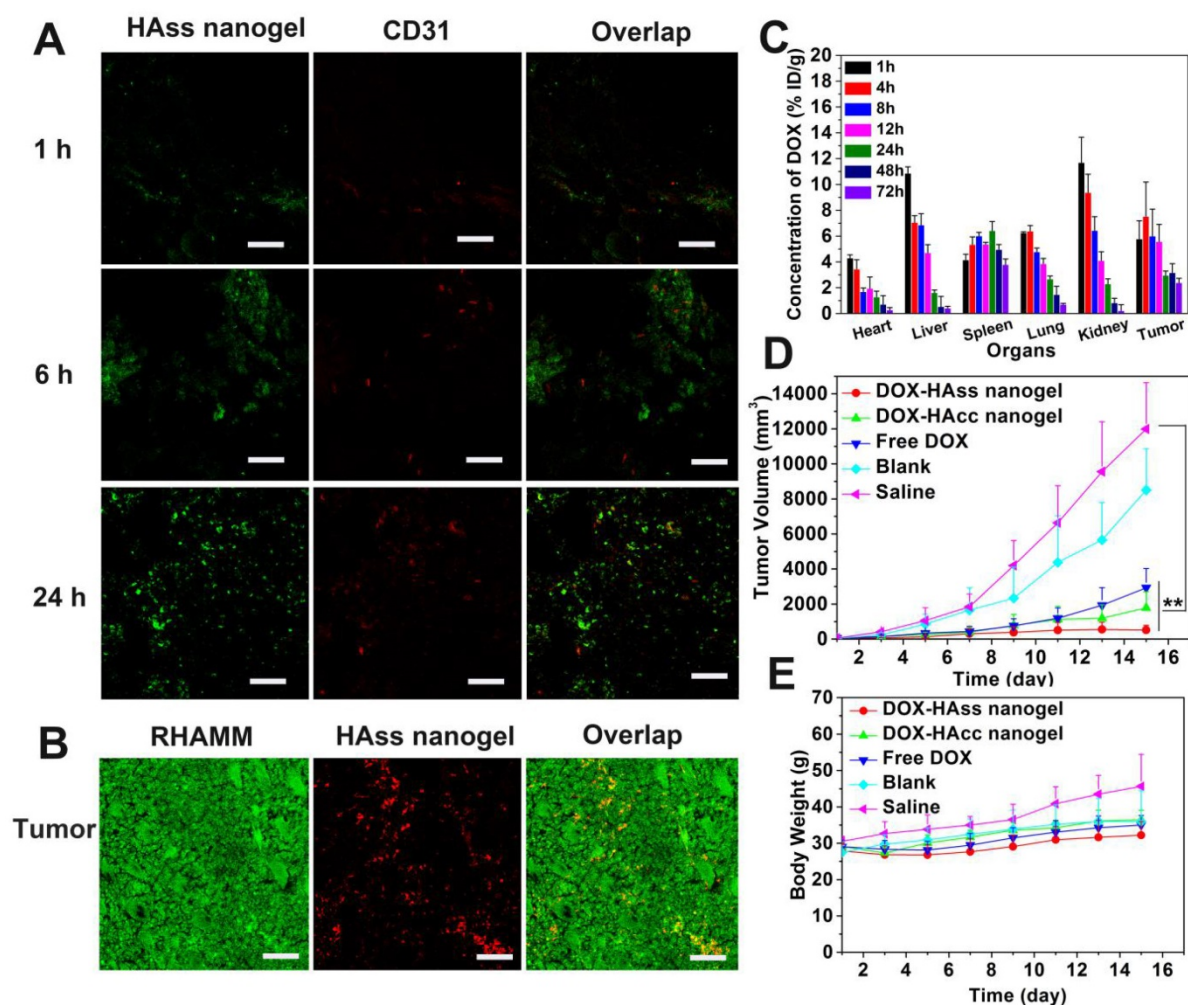


**Figure 5.** (A) Penetration of HAss nanogels in tumor at 1 h (up), 6 h (middle) and 24 h (bottom) post-injection. The scale bar is 100  $\mu\text{m}$ . (B) Immunofluorescence staining sections of RHAMM (green) expression in tumor, RBITC-HAss nanogels (red) penetrated in tumor at 24 h post-injection. All cell nuclei are not shown in this figure. The scale bar is 100  $\mu\text{m}$ . (C) Bio-distribution of DOX for DOX-loaded HAss nanogels in H22 subcutaneous tumor-bearing mice. The values were presented as the percentage of ID per gram of collected organs (mean  $\pm$  s.d.,  $n = 3$ ). (D) Tumor volume of the mice with different administrations as indicated (mean  $\pm$  s.d.,  $n = 10$ ). \*\* represents  $P < 0.01$ . (E) The weight plot of mice with different administrations (mean  $\pm$  s.d.,  $n = 10$ ).

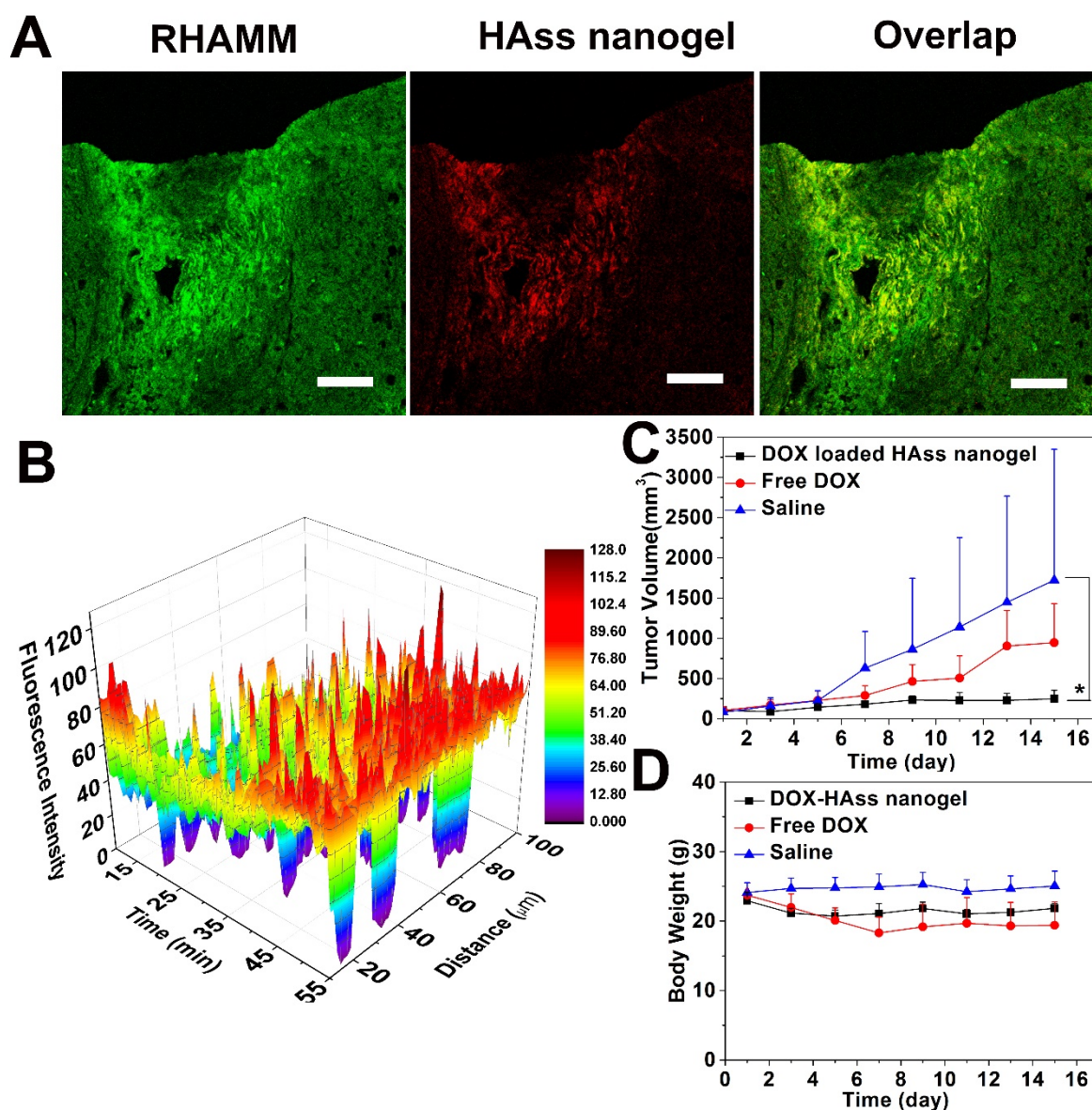


**Figure 6.** (A) Immunofluorescence staining sections of RHAMM (green) expression in LNCaP tumor tissue and RBITC-HAss nanogels (red) penetrated in tumor at 24 h post-injection. The cell nuclei are not shown in this figure. The scale bar is 100  $\mu\text{m}$ . (B) Plot of fluorescence intensity microdistribution of HAss nanogels at different times and different distances from vessel in LNCaP tumor tissue. The data are shown in three-dimensional diagram and the different fluorescence intensities are represented by different colors as shown in color histogram. (C) Tumor volume of LNCaP tumor-bearing nude mice that received different administrations as indicated (mean  $\pm$  s.d., n = 6). \* represents P < 0.05. (D) The weight plot of LNCaP tumor-bearing nude mice in different groups (mean  $\pm$  s.d., n = 6).

### **In vivo behavior of HA nanogels in LNCaP non-metastatic tumor model**

To further investigate RHAMM target mediated antitumor activity, we established another RHAMM-overexpressed animal model, that is, subcutaneous human prostate LNCaP tumor. The expression of RHAMM and the distribution of HAss nanogels in LNCaP tumor were examined. The LNCaP tumor-bearing mice were treated with RBITC-labeled HAss nanogels. At 24 h post-injection, then the mice were sacrificed and the tumor sections were stained with immunofluorescence. It can be seen that the RHAMM (green) is highly overexpressed in

LNCaP tumor and HAss nanogels (red) are well co-localized with RHAMM in the tumor tissue (Fig. 6A), demonstrating RHAMM-mediated tumor targeting of HA nanogels again.

*In vivo* real-time Near Infrared (NIR) fluorescence imaging observation was performed after i.v. injection of the NIR-797-labeled HAss nanogels into the nude mice with LNCaP tumor. The signal of HAss nanogels appears at the tumor site at 4 h post-injection, and become stronger and stronger with time (Fig. S16A). The *ex vivo* fluorescence intensity images of main organs and tissues at 24 h post-injection show that the fluorescence signal of HAss nanogels in the tumor is much higher than that

of heart, spleen, lungs, kidneys and brain but less than that of liver (Fig. S16B). The semi-quantitative data of NIR based on *ex vivo* fluorescence intensity images at 24 h post-injection reveal that the tumor accumulation of HAss nanogels reaches about 7% ID/g (Fig. S17) [36], indicating HA nanogels can significantly target to LNCaP tumor *in vivo*.

Similar to the mice with H22 tumor, we also explore the permeability of HAss nanogels in LNCaP tumor-bearing nude mice with the *in vivo* CLSM [37]. Fig. 6B shows the three-dimensional plot of *in vivo* permeation of HAss nanogels in LNCaP tumor. X-axle represents the time post-injection, Y-axle is designed as the distance from tumor vessel and Z-axle is indicated as fluorescence intensity. The red fluorescence signal of HAss nanogels is majorly found in the vessels in initial time, but the signals go far from the vessels as the observing time goes. Interestingly, the strong fluorescence signal can be found even in the distance of more than 100  $\mu\text{m}$  from the vessels, which is close to  $\text{O}_2$  diffusion limit distance from vessels [38]. This result fully demonstrates the great penetration capacity of HAss nanogels in LNCaP tumor. A probable explanation is that the relative small size and the strong RHAMM targeting of HA nanogels make them permeate deep in LNCaP tumor.

Next, the *in vivo* antitumor efficacy of DOX-loaded HAss nanogels in LNCaP tumor-bearing nude mice was examined with free DOX as positive control and saline as negative control. We can see that DOX-loaded HAss nanogels display remarkable antitumor activity compared to free DOX (Fig. 6C). On the 15<sup>th</sup> day, the average tumor size of the group treated by DOX-loaded HAss nanogels increases only 2.3 folds (v.s. 1<sup>st</sup> day), while the tumor sizes of the group received free DOX and saline increase 9.1 folds and 21.3 folds on the 15<sup>th</sup> day, respectively. The TGI values for free DOX and DOX-loaded HAss nanogels are 45% and 86%, respectively. And the differences of tumor volume are also highly statistical significant between DOX-loaded HAss nanogels and free DOX groups (both  $P < 0.05$ , Fig. 6C). The body weight measurements reveals that the body weights of group received the DOX-loaded HAss nanogels vary smoothly as the saline group, while the body weights of DOX group have an obvious decline, indicating that the DOX-loaded HAss nanogels have lower toxicity than free DOX *in vivo* (Fig. 6D).

### **In vivo behavior of HA nanogels in H22 metastatic tumor model**

Lymph node metastasis is a very frequent event at the terminal stage of various cancers, and it is one

of the greatest challenges in cancer treatment on account of the difficulty in drug delivery. Given that RHAMM is most likely to link with metastasis of tumor due to its motility and HA nanogels show highly tumor targeting mediated by RHAMM, H22 lymph node metastasis model was established by subcutaneously implanting H22 cells into the left rear paw of mice and then spontaneously developing metastases in the left inguinal lymph node to perform the following tests [39]. RHAMM expression in metastatic lymph node was first examined. As shown in the Fig. S18, the high expression of RHAMM (green) in H22 metastatic lymph node is confirmed. Meanwhile, the *ex vivo* permeation examination of HAss nanogels shows that a lot of HAss nanogels are diffused in H22 metastasis lymph node at 2 h after i.v. injection. Interestingly, these nanogels are hardly found in normal lymph nodes in the same mice (Fig. 7A). Then, the accumulation of HAss nanogels in metastatic lymph node was investigated by injecting NIR-797 labeled HAss nanogels into H22 metastasis mice intravenously. The real time *in vivo* NIR images are shown in the Fig. S19. After 72 h post-injection, the mice were sacrificed. Then the metastatic and normal lymph nodes were collected and imaged (Fig. 7B). We can see that the strong fluorescence signals of HAss nanogels appear in the H22 metastatic inguinal lymph nodes, suggesting that the HAss nanogels can reach there rapidly and stay there for a long time. Similarly, there is no significant fluorescence signal occurs in the healthful lymph nodes which are located in the same mice. These observations suggest that HAss nanogels can selectively accumulate in metastatic lymph nodes but not in healthful ones.

Then we examined whether HAss nanogels can carry DOX to metastatic lymph node and avoid the enrichment of DOX in normal lymph node through i.v. injection of DOX-loaded HAss nanogels. Interestingly, the bio-distribution of DOX in metastatic lymph node for the nanogel group reaches about 7.4% and 8.1% ID/g after 12 h and 24 h post-injection, respectively, while this value is about 1.8% and 1.5% ID/g in normal lymph node (Fig. 7C). In contrast, the DOX concentration in metastatic lymph node for free DOX group is only 1.3% and 0.6% ID/g at 12 h and 24 h post-injection (Fig. 7C). This means that the DOX concentration in metastatic lymph node for DOX-loaded HAss nanogels group is much higher than that of free DOX injected (about 5-fold,  $P < 0.01$ , Fig. 7C). These results indicate the HAss nanogels can selectively carry drug into lesion location rather than health lymph tissue.

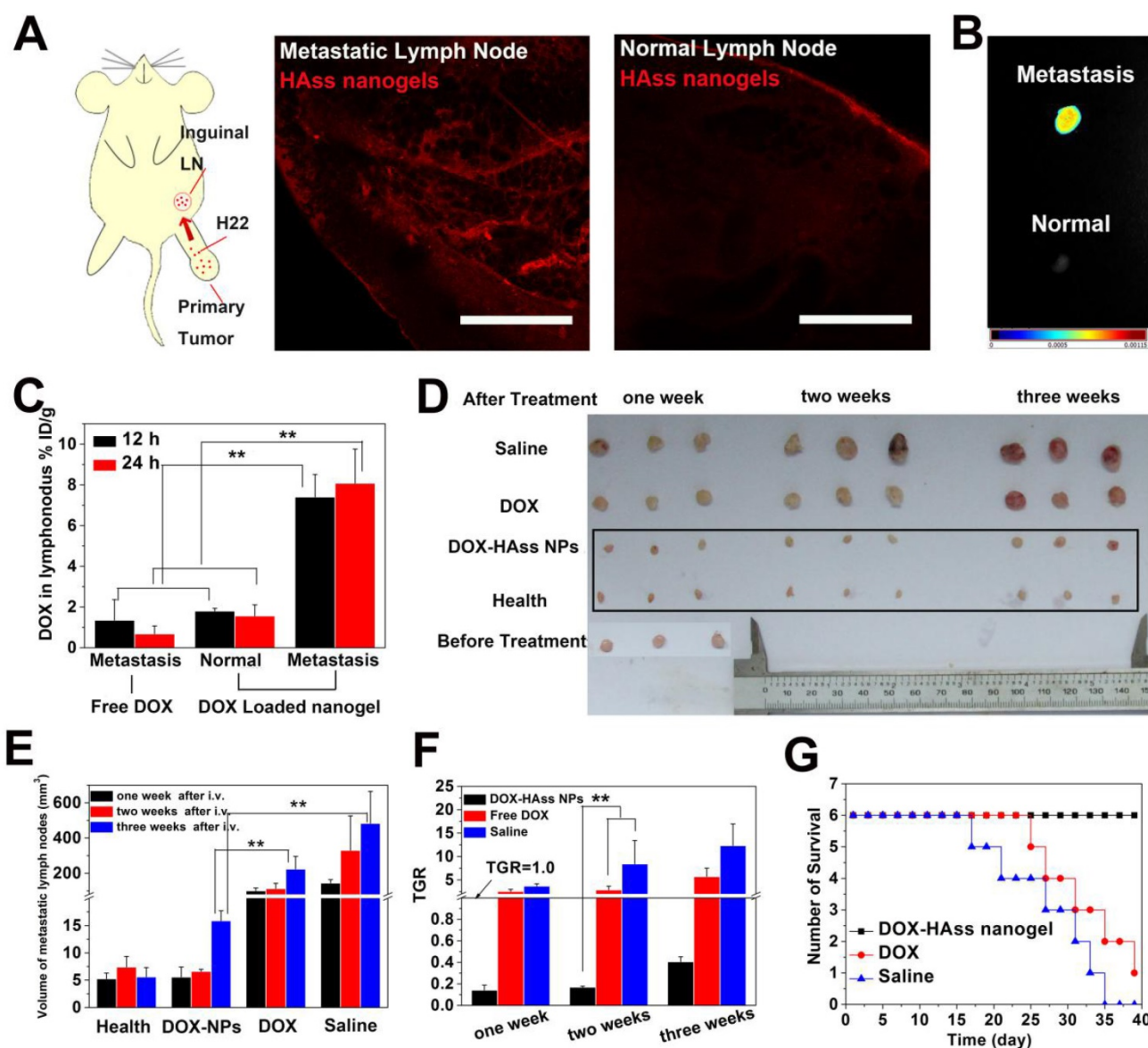


**Figure 7.** (A) Diagrammatic drawing of establishing lymph node metastases model in mouse and RBITC-HAss nanogels (red) penetrated in metastatic lymph node (left) and normal one (right) at 2 h post-injection *ex vivo*. The scale bar is 500  $\mu$ m. (B) *Ex vivo* NIR imaging of H22 metastatic lymph node (up) and health lymph node (bottom) following i.v. injection of NIR-797 labeled HAss nanogels. The different fluorescence intensities are represented by different colors as shown in color histogram. (C) Bio-distribution of DOX in lymph node for DOX or DOX-loaded HAss nanogels groups in the mice with H22 lymphatic metastasis at various time points post-injection. The results were presented as % ID/g (n = 3). (D) The photograph of the sizes of lymph node at one week, two weeks and three weeks after treated with saline, DOX and DOX loaded HAss nanogels, respectively. (E) Quantitative statistics of lymph node sizes and (F) tumor growth rate (TGR) of lymph node. The black parallel line represents the TGR = 1.0. All above data are represented as mean  $\pm$  s.d. (n = 3). \*\* represents P < 0.01. (G) Survival curves of H22 lymphatic metastasis mice with different treatments (n = 6).

We next investigated the inhibition of DOX-loaded HAss nanogels to the metastasis in lymph node by intravenously injecting them into metastases-bearing mice without excising primary tumors. We can see that the inhibition of DOX-loaded HAss nanogels to the metastatic lymph node is fully effective (Fig. 7D-7F). The size of metastatic lymph node becomes the same as that of health lymph node after one week and two weeks injection, and increases slightly at three weeks post-injection (Fig. 7D). Compared with saline control, the inhibition rates of DOX-loaded HAss nanogel group are 96%, 98% and

97%, at one week, two weeks and three weeks, respectively (Fig. 7E). Compared with that before treatment, the size of metastatic lymph node decreases 86%, 83%, 59% at one, two and three weeks for the group received DOX-loaded HAss nanogels. The tumor growth rate (TGR) of DOX-loaded HAss nanogels group at one, two and three weeks is 0.14, 0.16 and 0.40 (Fig. 7F), respectively, all less than 1.0, which means that the metastasis is nearly healed. In contrast, the size of metastatic lymph node increases 156%, 188%, 457% for the group received free DOX (TGR is 2.57, 2.88 and 5.71 respectively) and 269%,

742%, 1132% for the group treated with saline (TGR is 3.69, 8.42 and 12.32 respectively), respectively. The TGR of both free DOX and saline groups are greater than 1.0. It indicates that the metastasis occurs continuously and the H22 tumor in lymph node keeps growing. The survival time of metastases-bearing mice shows that all mice die in the group treated by saline during the 35 days post-injection, and only one mouse survived for the group treated by free DOX during 40 days post-injection. Encouragingly, no mouse dies in the group treated by DOX-loaded HAss nanogels during the whole observation period (Fig. 7G). These results demonstrate clearly that DOX-loaded HAss nanogels can well inhibit the growth of metastatic lymph node, even completely heal malignant lymph node metastasis and significantly prolong the survival time of metastases-bearing mice.

## Conclusion

In summary, we have prepared a bio-reductive sensitive HA nanogels for targeting delivery of DOX to both subcutaneous tumors and metastatic lesions which have over-expressed RHAMM. The HA nanogels cross-linked with disulfide linkages had a stable particle structure but disintegrated and selectively released DOX loaded in reductive environments. The *in vitro* cellular uptake and cytotoxicity evaluation showed that DOX-loaded HA nanogels had a noteworthy affinity to RHAMM overexpressed cancer cells and much higher cytotoxicity than free DOX. *In vivo* antitumor activity examinations demonstrated that the excellent antitumor activity of DOX-loaded HAss nanogels was owed to their strong RHAMM targeting, deep tumor permeation, high drug accumulation, large RHAMM-mediated uptake of cancer cells and the sensitivity of HA nanogels in reductive tumor microenvironment. The drug delivery of lymph node metastasis by systemically administering DOX-loaded HA nanogels demonstrated that the HA nanogels could specifically transport drug to metastatic lymph node through RHAMM-HA interaction and inhibit the growth of metastatic lymph node, even completely heal malignant lymph node metastasis. Thus, RHAMM-directed drug delivery is a promising therapy route for treating both primary and metastatic tumors.

## Abbreviations

RHAMM: receptor for hyaluronic acid mediated motility; HA: hyaluronic acid; EPR: enhanced permeation and retention; ICAM-1: intercellular adhesion molecule 1; FITC: fluorescein isothiocyanate; IgG: immunoglobulin G; DOX: doxorubicin; GSH:

glutathione; DOX: doxorubicin; MBA: *N*, *N'*-methylene bisacrylamide; RBITC: rhodamine B isothiocyanate; FBS: fetal bovine serum; MAHA: methacrylated hyaluronic acid; CBA: cystamine bisacrylamide; DS: degree of substitution; MA: methacrylic; D<sub>2</sub>O: deuterium oxide; HAss nanogels: Redox-responsive nanogels; HAcc nanogels: non-Redox-responsive nanogels; DLS: dynamic light scattering; TEM: Transmission electron microscopy; PBS: phosphate buffered saline; MTT: 1-(4,5-dimethylthiazol-2-yl)-3,5-diphenyl-formazan; DL: drug loading; CLSM: confocal laser scanning microscope; NIR: near infrared; BSA: bovine serum albumin; EE: encapsulation efficiency; EDTA: edetic acid; TGI: tumor growth inhibition; FACS: fluorescence-activated cell sorting; I.V.: intravenous; O. C. T.: optimum cutting temperature; ROI: region of interest; IAS: inhalational anaesthesia system; TGR: tumor growth rate; ID: injection dose; AB: antibody.

## Supplementary Material

Part of Experimental Section, Scheme S1, Figure S1-S19. <http://www.thno.org/v07p1719s1.pdf>

## Acknowledgments

This work was supported by the Natural Science Foundation of China (No. 51690153, 21474045 and 51422303), the Specialized Research Fund for the Doctoral Program of Higher Education, and the Program for Changjiang Scholars and Innovative Research Team in University.

## Competing Interests

The authors have declared that no competing interest exists.

## References

1. Singh R, Lillard JW. Nanoparticle-based targeted drug delivery. *Exp Mol Pathol.* 2009; 86: 215-223.
2. Chen K, Chen X. Integrin Targeted Delivery of Chemotherapeutics. *Theranostics.* 2011; 1: 189-200.
3. Yu MK, Park J, Jon S. Targeting Strategies for Multifunctional Nanoparticles in Cancer Imaging and Therapy. *Theranostics.* 2012; 2 (1): 3-44.
4. Turley EA, Noble PW, Bourguignon LYW. Signaling properties of hyaluronan receptors. *J Biol Chem.* 2002; 277: 4589-4592.
5. Zhang SW, Chang MCY, Zylka D, Turley S, Harrison R, Turley EA. The hyaluronan receptor RHAMM regulates extracellular-regulated kinase. *J Biol Chem.* 1998; 273: 11342-11348.
6. Goueffic Y, Guilly C, Guerin P, Patra P, Pacaud P, Loirand G. Hyaluronan induces vascular smooth muscle cell migration through RHAMM-mediated PI3K-dependent Rac activation. *Cardiovasc Res.* 2006; 72: 339-348.
7. Tolg C, Hamilton SR, Nakrieko KA, Kooshesh F, Walton P, McCarthy JB, Bissell MJ, Turley EA. Rhamm(-/-) fibroblasts are defective in CD44-mediated ERK1,2 mitogenic signaling, leading to defective skin wound repair. *J Cell Biol.* 2006; 175: 1017-1028.
8. Zaman A, Cui Z, Foley JP, Zhao HJ, Grimm PC, DeLisser HM, Savani RC. Expression and role of the hyaluronan receptor RHAMM in inflammation after bleomycin injury. *Am J Respir Cell Mol Biol.* 2005; 33: 447-454.
9. Turley EA, Austen L, Moore D, Hoare K. Ras-transformed cells express both CD44 and RHAMM hyaluronan receptors - only RHAMM is essential for hyaluronan-promoted locomotion. *Exp Cell Res.* 1993; 207: 277-282.
10. Li H, Guo L, Li JW, Liu N, Qi R, Liu J. Expression of hyaluronan receptors CD44 and RHAMM in stomach cancers: relevance with tumor progression. *Int J Oncol.* 2000; 17: 927-932.

11. Gurski LA, Jha AK, Zhang C, Jia X, Farach-Carson MC. Hyaluronic acid-based hydrogels as 3D matrices for in vitro evaluation of chemotherapeutic drugs using poorly adherent prostate cancer cells. *Biomaterials*. 2009; 30: 6076-6085.
12. Hamilton SR, Fard SF, Paiwand FF, Tolg C, Veishe M, Wang C, McCarthy JB, Bissell M J, Koropatnick J, Turley EA. The hyaluronan receptors CD44 and Rhamm (CD168) form complexes with ERK1,2 that sustain high basal motility in breast cancer cells. *J Biol Chem*. 2007; 282:16667-16680.
13. Gibbs P, Brown TJ, Ng R, Jennens R, Cinc E, Pho M, Michael M, Fox RM. a Pilot Human Evaluation of a Formulation of Irinotecan and Hyaluronic Acid in 5-Fluorouracil-Refractory Metastatic Colorectal Cancer Patients. *Chemotherapy*. 2009; 55: 49-59.
14. Augustin F, Fiegl M, Schmid T, Pomme G, Sterlacci W, Tzankov A. Receptor for hyaluronic acid-mediated motility (RHAMM, CD168) expression is prognostically important in both nodal negative and nodal positive large cell lung cancer. *J Clin Pathol*. 2015; 68: 368-373.
15. Greiner J, Schmitt A, Giannopoulos K, Rojewski MT, Goetz M, Funk I, Ringhoffer M, Bunjes D, Hofmann S, Ritter G, Doehner H, Schmitt M. High-dose RHAMM-R3 peptide vaccination for patients with acute myeloid leukemia, myelodysplastic syndrome and multiple myeloma. *Haematologica*. 2010; 95: 1191-1197.
16. Koelzer VH, Huber B, Mete V, Iezzi G, Trippel M, Karamitopoulou E, Zlobec I, Lugli A. Expression of the hyaluronan-mediated motility receptor RHAMM in tumor budding cells identifies aggressive colorectal cancers. *Hum Pathol*. 2015; 46:1573-1581.
17. Du YCN, Chou CK, Klimstra DS, Varmus H. Receptor for hyaluronan-mediated motility isoform B promotes liver metastasis in a mouse model of multistep tumorigenesis and a tail vein assay for metastasis. *Proc Natl Acad Sci USA*. 2011; 108: 16753-16758.
18. Schmitt M, Schmitt A, Rojewski MT, Chen J, Giannopoulos K, Fei F, Yu Y, Goetz M, Heyduk M, Ritter G, Speiser DE, Grjatic S, Guillaume P, Ringhoffer M, Schlenk RF, Liebisch P, Bunjes D, Shiku H, Dohner H, Greiner J. RHAMM-R3 peptide vaccination in patients with acute myeloid leukemia, myelodysplastic syndrome, and multiple myeloma elicits immunologic and clinical responses. *Blood*. 2008; 111: 1357-1365.
19. Misra S, Hascall VC, Markwald RR, Ghatak S. Interactions between hyaluronan and its receptors (CD44, RHAMM) regulate the activities of inflammation and cancer. *Front Immun*. 2015; 6.
20. Turley EA, Naor D. RHAMM and CD44 peptides-analytic tools and potential drugs. *Front Biosci*. 2012; 17: 1775-1794.
21. Giannopoulos K, Dmoszynska A, Kowal M, Rolinski J, Gostick E Price DA, Greiner J, Rojewski M, Stilgenbauer S, Dohner H, Schmitt M. Peptide vaccination elicits leukemia-associated antigen-specific cytotoxic CD8+ T-cell responses in patients with chronic lymphocytic leukemia. *Leukemia*. 2010; 24: 798-805.
22. Gust KM, Hofer MD, Perner SR, Kim R, Chinnaiyan AM, Varambally S, Moller P, Rinnab L, Rubin MA, Greiner J, Schmitt M, Kuefer R, Ringhoffer M. RHAMM (CD168) is Overexpressed at the Protein Level and May Constitute an Immunogenic Antigen in Advanced Prostate Cancer Disease. *Neoplasia*. 2009; 11: 956-963.
23. Lin SL, Chang D, Chiang A, Ying SY. Androgen receptor regulates CD168 expression and signaling in prostate cancer. *Carcinogenesis*. 2008; 29: 282-290.
24. Snauwaert S, Vanhee S, Goetgeluk G, Verstichel G, Van Caeneghem Y, Velghe I, Philippe J, Berneman ZN, Plum J, Taghon T, Leclercq G, Thielemans K, Kerre T, Vandekerckhove B. RHAMM/HMMR (CD168) is not an ideal target antigen for immunotherapy of acute myeloid leukemia. *Haematologica*. 2012; 97: 1539-1547.
25. Nikitovic D, Tzardi M, Berdiaki A, Tsatsakis A, Tzanakakis G. Cancer microenvironment and inflammation: role of hyaluronan. *Front Immun*. 2015; 6.
26. Heldin P, Basu K, Olofsson B, Porsch H, Kozlova I, Kahata K. Deregulation of hyaluronan synthesis, degradation and binding promotes breast cancer. *J Biochem*. 2013; 154: 395-408.
27. Schmitt A, Barth TFE, Beyer E, Borchert F, Rojewski M, Chen J, Guillaume P, Gronau S, Greiner J, Moeller P, Riechelmann H, Schmitt M. The tumor antigens RHAMM and G250/CAIX are expressed in head and neck squamous cell carcinomas and elicit specific CD8(+) T cell responses. *Int J Oncol*. 2009; 34: 629-639.
28. Zhu Z, Xie C, Liu Q, Zhen X, Zheng X, Wu W, Li R, Ding Y, Jiang X, Liu B. The effect of hydrophilic chain length and iRGD on drug delivery from poly( $\epsilon$ -caprolactone)-poly(N-vinylpyrrolidone) nanoparticles. *Biomaterials*. 2011; 32: 9525-9535.
29. Wu W, Driessen W, Jiang XQ. Oligo(ethylene glycol)-Based Thermosensitive Dendrimers and Their Tumor Accumulation and Penetration. *J Am Chem Soc*. 2014; 136: 3145-3155.
30. Bladou F, Vessella RL, Buhler KR, Ellis WJ, True LD, Lange PH. Cell proliferation and apoptosis during prostatic tumor xenograft involution and regrowth after castration. *Int J Cancer*. 1996; 67: 785-790.
31. Grazon C, Rieger J, Sanson N, Charleux B. Study of poly(N, N-diethylacrylamide) nanogel formation by aqueous dispersion polymerization of N, N-diethylacrylamide in the presence of poly(ethylene oxide)-b-poly(N, N-dimethylacrylamide) amphiphilic macromolecular RAFT agents. *Soft Matter*. 2011; 7: 3482-3490.
32. Qiao ZY, Zhang R, Du FS, Liang DH, Li ZC. Multi-responsive nanogels containing motifs of ortho ester, oligo(ethylene glycol) and disulfide linkage as carriers of hydrophobic anti-cancer drugs. *J Control Release*. 2011; 152: 57-66.
33. Kuppasamy P, Li HQ, Ilangovan G, Cardounel AJ, Zweier JL, Yamada K, Krishna MC, Mitchell JB. Noninvasive imaging of tumor redox status and its modification by tissue glutathione levels. *Cancer Res*. 2002; 62: 307-312.
34. Schafer FQ, Buettner GR. Redox environment of the cell as viewed through the redox state of the glutathione disulfide/glutathione couple. *Free Radical Biol Med*. 2001; 30: 1191-1212.
35. Qian H, Wang X, Yuan K, Xie C, Wu W, Jiang X, Hu L. Delivery of doxorubicin in vitro and in vivo using bio-reductive cellulose nanogels. *Biomater Sci* 2014; 2: 220-232.
36. Gao J, Chen K, Xie R, Xie J, Yan Y, Cheng Z, Peng X, Chen X. In Vivo Tumor-Targeted Fluorescence Imaging Using Near-Infrared Non-Cadmium Quantum Dots. *Bioconju Chem*. 2010; 21: 604-609.
37. Li HJ, Du JZ, Du XJ, Xu CF, Sun CY, Wang HX, Cao ZT, Yang XZ, Zhu YH, Nie SM, Wang J. Stimuli-responsive clustered nanoparticles for improved tumor penetration and therapeutic efficacy. *Proc Natl Acad Sci USA*. 2016; 113: 4164-4169.
38. Gatenby RA, Gillies RJ. Why do cancers have high aerobic glycolysis? *Nat Rev Cancer*. 2004; 4: 891-899.
39. Liang C, Diao S, Wang C, Gong H, Liu T, Hong G, Shi X, Dai H, Liu Z. Tumor Metastasis Inhibition by Imaging-Guided Photothermal Therapy with Single-Walled Carbon Nanotubes. *Adv Mater*. 2014; 26: 5646-+.